

Nonlinear Bloch waves in metallic photonic band-gap filaments

Artan Kaso* and Sajeev John

Department of Physics, University of Toronto, 60 St. George Street, Toronto, Ontario, Canada M5S 1A7

(Received 21 August 2007; published 30 November 2007)

We demonstrate the occurrence of nonlinear Bloch waves in metallic photonic crystals (PCs). These periodically structured filaments are characterized by an isolated optical pass band below an effective plasma gap. The pass band occurs in a frequency range where the metallic filament exhibits a negative, frequency-dependent dielectric function and absorption loss. The metallic losses are counterbalanced by gain in two models of inhomogeneously broadened nonlinear oscillators. In the first model, we consider close-packed quantum dots that fill the void regions of a two-dimensional (2D) metallic PC, and whose inhomogeneously broadened emission spectrum spans the original optical pass band of the bare filament. In the second model, we consider thin (10–50 nm) layers of inhomogeneously broadened two-level resonators, with large dipole oscillator strength, that cover the interior surfaces of 2D metallic (silver and tungsten) PCs. These may arise from localized surface plasmon resonances due to small metal particles or an otherwise rough metal surface. For simplicity, we treat electromagnetic modes with electric field perpendicular to the plane of metal periodicity. In both models, a pumping threshold of the resonators is found, above which periodic nonlinear solutions of Maxwell's equations with purely real frequency within the optical pass band emerge. These nonlinear Bloch waves exhibit a laserlike input pumping to output amplitude characteristic. For strong surface resonances, these nonlinear waves may play a role in light emission from a hot tungsten (suitably microstructured) filament.

DOI: [10.1103/PhysRevA.76.053838](https://doi.org/10.1103/PhysRevA.76.053838)

PACS number(s): 42.70.Qs, 42.55.Tv

I. INTRODUCTION

The interference of scattered electromagnetic waves gives rise to the fundamental phenomenon of light localization under suitable circumstances [1,2]. In certain types of photonic crystals (PCs), this is facilitated by the emergence of a photonic band gap (PBG) [2,3], where optical pathways for escape from a trapping center are eliminated by destructive interference. An important consequence of light localization [2] is the elimination of ordinary spontaneous emission [3,4] from atoms or quantum dots and the formation of photon-atom bound states [5,6]. In free space the density of electromagnetic modes is proportional to the frequency squared. In PCs with photonic band gaps, spectral regions surrounding the PBG may experience an enhanced density of states (DOS), where many more modes than in free space are available for propagation. This engineering of the density of electromagnetic modes has applications ranging from optical switching in dielectric structures [7,8] to exceptional thermal light emission in metallic PBG filaments [9–11].

Metallic photonic crystals may exhibit a large spectral gap at low frequencies without recourse to scattering and interference mechanisms. In a bulk metal, mobile charge carriers can screen out electromagnetic waves at frequencies below the plasma frequency [12]. When such a metal is periodically structured with void regions in the form of a photonic crystal filament, a lower effective plasma frequency exists [13], below which electromagnetic propagation is screened out. The resulting photonic band gap results from a combination of plasma screening effects and Bragg scattering. Tungsten-based PBG filaments of this type have been studied in both the woodpile geometry [9–11] and the inverse opal geometry

[14]. An intriguing possibility with metallic PBG filaments is the engineering of a sharply defined optical pass band below the effective plasma screening frequency [15]. This electromagnetic pass band arises from the periodic network of void regions in the PBG filament, enabling light to propagate largely through air and to avoid the screening electrons of the metallic filament. This optical pass band can provide a narrow-transmission band while the remainder of the plasmonic PBG acts as a filter for other frequencies of radiation.

Within the interior of a PBG filament, the optical pass band is a spectral region where the electromagnetic density of states acquires a very large value, surrounded by a broad band of nearly vanishing mode density. It is of interest to study the behavior of internal light emitters that couple to modes in such an optical pass band. One possibility is through intentionally placed colloidal quantum dots that are infiltrated within the void regions of the microstructured metallic filament. Another source of light emission may arise from unintentional localized plasmonic resonators that form on the interior surfaces of the metal during the synthesis of the filament. These may take the form of small metal particles that contribute to metal surface roughening. Recently, a striking interplay was observed between localized plasmonic resonances due to small particles [created during a sputtering process for fabrication of one-dimensional (1D) metal gratings] and extended surface plasma waves on the grating [16,17]. In an electrically pumped metallic filament, such resonators could be excited and emit light, over and above thermal, blackbody radiation. Thermal light emission generated by electrical pumping and heating of the metallic PBG filament may exhibit exceptional intensity in the spectral range of such a pass band.

Experimental studies have revealed spectral selection of thermal radiation generated by high-temperature microstructured metallic (tungsten) PCs [9–11] and metallic surfaces [18] even in the absence of optical pass band engineering. In

*akaso@physics.utoronto.ca

the case of metallic PCs, thermal light spectral features very distinct from standard blackbody radiation are observed, showing peaks at frequencies corresponding to structural features of the underlying PC. These peaks become more pronounced as the temperature of the metallic structure is increased, suggesting a nonlinear or threshold phenomenon over and above the linear electromagnetic band structure effects. A more complete picture of radiation from thermally excited filaments can be obtained by considering both the response of an inhomogeneously broadened distribution of dipole resonators within the light-emitting filament and the multidirectional feedback mechanism provided from the underlying PC. This situation lies within the purview of the nonlinear Bloch wave method introduced recently [19] to describe resonant nonlinear photonic crystals with a complex, frequency-dependent dielectric function.

In this paper, we demonstrate the existence of nonlinear Bloch waves for the case of a metallic backbone PC where the real part of the dielectric function is both negative and frequency dependent, and the imaginary part of the dielectric function is also considered. For simplicity, we restrict our numerical studies to 2D metallic PCs where the electric field vector is everywhere perpendicular to the plane of periodicity (E polarization). Our previous analysis [19] considered materials where the real part of the dielectric constant of the combined system (backbone PC plus the nonlinear resonators) was strictly positive at all frequencies. This restriction was respected in order to achieve rapid convergence of our iterative, self-consistent method. If, on the other hand, the dielectric constant of one component of a two-component PC is negative, the plane wave expansion (PWE) method yields an “indefinite” matrix whose eigenvalues ω^2/c^2 are formally either positive or negative. The linear band structure of the metallic PC can, in principle, be constructed keeping only the physical, positive eigenvalues. This straightforward application of the PWE method to negative dielectrics produces a stable photonic band structure for the 2D E polarization case. However, the band structure obtained for the 2D H polarization (magnetic field vector perpendicular to the plane of periodicity) is highly unstable (depending sensitively on the number of plane waves employed). This may be a consequence of the existence of surface plasmon modes, strongly localized along the interior surfaces of the metallic PC, which are not efficiently represented by a small finite sum of plane wave states.

Negative values of the dielectric are possible only for a frequency-dependent response of the material to the applied electromagnetic fields. The dielectric response of an idealized metal has the Drude frequency dependence $1 - \omega_p^2/\omega(\omega + i\tau^{-1})$. In the Drude model, ω_p is the plasma frequency and τ is the average collision time of free electrons. For ideal conductors $\tau \rightarrow \infty$ and can be dropped altogether from the metallic dielectric function. Then the dielectric function is negative for frequencies below the plasma frequency. The frequency dependence of the dielectric response leads to an eigenvalue problem in which the matrix obtained from the PWE method depends on the eigenvalue itself. The resulting eigenvalue problem is no longer linear. The cutting surface method (CSM) [15] approaches this nonlinear problem by solving a family of related linear systems described

by a continuum of *constant* negative dielectrics in the metallic region. As the negative value is varied over a reasonable range, photonic band surfaces are obtained using the PWE method. The true eigenfrequencies, allowed from the frequency-dependent dielectric, are found by intersection of the band surfaces with the frequency-dependent dielectric function (cutting surface). The resulting band structure obtained by the CSM for an ideal Drude conductor agrees very well with that obtained independently by Kuzmiak *et al.* [13].

In the approach of Kuzmiak *et al.*, the Drude dielectric response of the metal is incorporated into the PWE method. For the specific frequency dependence $1 - \omega_p^2/\omega^2$, a linearization of the eigenvalue problem ensues. The approach of Kuzmiak *et al.* is elegant but highly specialized. The CSM, on the other hand, can treat a background dielectric different from unity and other non-Drude functional forms of the dielectric response of the metallic regions, assuming this response is linear and contains no losses (or gain).

In this paper, we modify the nonlinear Bloch wave method introduced earlier for positive dielectrics [19], by incorporating the Drude response of the metallic regions from the outset, following the approach of Kuzmiak *et al.* We focus on the technically simple case of 2D E polarization in a metallic backbone photonic crystal (BPC) and we generalize the nonlinear Bloch wave method to treat an incoherently pumped, inhomogeneously broadened distribution of two-level resonators that either fill the voids of the metallic PC or form a thin coating on the interior surfaces of a metallic PC. For concreteness, we consider a square lattice of metallic rods of circular cross section, with a realistic complex dielectric function taken from experimental data. These metallic rods allow for a connected network of voids that enable an isolated optical pass band below the effective plasma frequency of the filament. The 2D H polarization case will be the object of future work.

This paper is organized as follows. In Sec. II we formulate equations for determining the Drude backbone photonic crystal (BPC) normal modes and we discuss their normalization. In Secs. III and IV we extend the nonlinear Bloch wave method for negative dielectric BPCs. In Sec. V we numerically verify the validity of our self-consistent nonlinear integral equation for Bloch modes by applying it to the simple case when the nonmetallic void regions have a uniform, linear, frequency-independent dielectric constant different from unity. In Sec. VI we apply our method to a realistic non-Drude dielectric backbone PC with values taken from experimental data. The space between metallic rods is modeled with various coatings of nonlinear oscillators capable of emitting and absorbing light in the spectral vicinity of the optical pass band. The optical response of the inhomogeneously broadened collection of the emitters is described by a complex, frequency-dependent, nonlinear susceptibility. We observe that for sufficient incoherent pumping (from either electrical or other heat sources) self-consistent Bloch waves emerge whose amplitude exhibits a threshold behavior with pumping. The threshold pumping for these nonlinear Bloch waves (with purely real frequency and nondecaying amplitude) in this dissipative medium depends on the density of resonators, their dipole oscillator strength, and their volume filling fraction in the filament.

II. BASIS STATES OF A METALLIC BACKBONE PHOTONIC CRYSTAL

For the backbone of our system, we consider a 2D metallic photonic crystal in which the imaginary part of the dielectric function is initially neglected. This allows us to identify suitable basis functions for the treatment of nonlinear dielectric components added to this metallic backbone as well as the imaginary (loss or gain) part of the overall dielectric function.

We define z as the direction perpendicular to the plane of periodicity of the crystal, and we denote $\vec{E}=(0,0,E)$ and $\vec{H}=(H_x,H_y,0)$ as the electric and magnetic fields, respectively, for an electromagnetic wave polarized along the z axis. Maxwell's curl equations can be expressed as

$$\partial_x H_y - \partial_y H_x = -\frac{i\omega}{c}\epsilon(\vec{r})E \quad \text{and} \quad \vec{\nabla}E = -\frac{i\omega}{c}(H_y, -H_x),$$

where \vec{r} is the two-dimensional vector in the plane of periodicity, $\vec{r}=x\hat{x}+y\hat{y}$, and $\vec{\nabla}=\hat{x}\partial/\partial x+\hat{y}\partial/\partial y$. The eigenvalue problem of the 2D PC is formulated in terms of the electric field E , by eliminating H_x and H_y from the above:

$$\nabla^2 E + \frac{\omega^2}{c^2}\epsilon(\vec{r})E = 0 \quad (1)$$

It is useful to introduce a step function

$$\theta_M(\vec{r}) = \begin{cases} 1 & \text{in metallic regions,} \\ 0 & \text{otherwise,} \end{cases} \quad (2)$$

in order to separate the metallic and void regions of the PC filament. Let $\epsilon_a(\omega)=\epsilon_0-\omega_p^2/\omega^2$ be the real part of the dielectric function of a Drude-type metal and let ϵ_b represent the *real, positive* dielectric constant of the other component. The position-dependent dielectric function of the photonic crystal is then given by $\epsilon(\vec{r})=\epsilon_b+[\epsilon_a(\omega)-\epsilon_b]\theta_M(\vec{r})$. This can alternatively be expressed as

$$\epsilon(\vec{r}) = \epsilon_{\text{BPC}}(\vec{r}) + 4\pi\chi_\omega(\vec{r}), \quad (3a)$$

where

$$\epsilon_{\text{BPC}}(\vec{r}) = \epsilon_b - (\omega_p^2/\omega^2)\theta_M(\vec{r}) \quad (3b)$$

and

$$4\pi\chi_\omega(\vec{r}) = (\epsilon_0 - \epsilon_b)\theta_M(\vec{r}). \quad (3c)$$

We refer to $\epsilon_{\text{BPC}}(\vec{r})$ as the dielectric function of the backbone photonic crystal, whereas $4\pi\chi_\omega(\vec{r})$ is considered as a ‘‘perturbation.’’ The BPC can then be treated using the approach of Kuzmiak *et al.* For the purpose of defining basis functions, we consider the wave equation for the backbone PC,

$$\nabla^2 E - \frac{\omega_p^2}{c^2}\theta_M(\vec{r})E + \frac{\omega^2}{c^2}\epsilon_b E = 0. \quad (4)$$

Equation (4) is self-adjoint and its solutions are orthogonal Bloch modes of the form $E_\omega(\vec{r})=e^{i\vec{k}\cdot\vec{r}}u(\vec{r})$, where $u(\vec{r})=\sum_{\vec{G}}\tilde{u}(\vec{G})e^{i\vec{G}\cdot\vec{r}}$ has the periodicity of the direct lattice. Here \vec{k} is the Bloch wave vector from the first Brillouin zone. The

eigenmodes $\psi_{\vec{k},l}(\vec{r})$ of Eq. (4), with band index l , have eigenvalues $\omega=\omega_{\vec{k},l}$ and, upon suitable normalization (see the Appendix) satisfy the orthonormality condition

$$\frac{1}{\mathcal{V}}\int_{\mathcal{V}} d^2r \psi_{\vec{q},n}^*(\vec{r})\psi_{\vec{k},l}(\vec{r})\epsilon_{\vec{k},l}(\vec{r}) = \delta_{\vec{q},\vec{k}}\delta_{n,l}, \quad (5)$$

where $\epsilon_{\vec{k},l}(\vec{r})\equiv\epsilon_b-(\omega_p^2/\omega_{\vec{k},l}^2)\theta_M(\vec{r})$. This can be expressed as

$$\frac{1}{\mathcal{V}}\int_{\mathcal{V}} d^2r \psi_{\vec{q},n}^*(\vec{r})\psi_{\vec{k},l}(\vec{r})\epsilon_b = a_{\vec{k},l}\delta_{\vec{q},\vec{k}}\delta_{n,l}, \quad (6a)$$

where

$$a_{\vec{k},l}\equiv\left(1+\frac{\omega_p^2}{\omega_{\vec{k},l}^2}\frac{1}{\mathcal{V}}\int_{\mathcal{V}} d^2r \psi_{\vec{k},l}^*(\vec{r})\psi_{\vec{k},l}(\vec{r})\theta_M(\vec{r})\right), \quad (6b)$$

and the integration is over the whole two-dimensional volume \mathcal{V} of the photonic crystal. In metallic regions, for frequencies $\omega_{\vec{k},l}<\omega_p$, the dielectric function $\epsilon_{\vec{k},l}(\vec{r})$ is negative. Here, the fields $\psi_{\vec{k},l}(\vec{r})$ do not penetrate deeply into the metallic regions. The eigenmodes $\psi_{\vec{k},l}(\vec{r})$ nevertheless form a complete basis, and an arbitrary electric field, polarized perpendicular to the plane of periodicity, can be written as

$$E(\vec{r}) = \sum_{\vec{k},l} f_{\vec{k},l}\psi_{\vec{k},l}(\vec{r}). \quad (7)$$

This expansion is suitable for describing more general Bloch waves arising from complex, nonlinear modifications to the void regions surrounding the metallic backbone PC and for non-Drude modifications of the backbone itself.

III. GREEN'S FUNCTION OF METALLIC BACKBONE PHOTONIC CRYSTAL

With the addition of a general complex susceptibility to the backbone PC described above, Eq. (1) for the E -polarized field becomes

$$\nabla^2 E_\omega(\vec{r}) + \frac{\omega^2}{c^2}[\epsilon_{\text{BPC}}(\vec{r}) + 4\pi\chi_\omega(\vec{r})]E_\omega(\vec{r}) = 0. \quad (8)$$

In general, the perturbation $4\pi\chi_\omega(\vec{r})$ is a nonlinear, spatially varying, complex function of frequency and it can occupy any region of space. In this section, we construct an exact integral equation formulation of the wave equation in which the Green's function kernel describes the relevant properties of the BPC and the complex, nonlinear perturbation causes further multiple scattering. This integral equation must, in general, be solved by an iterative technique that leads to self-consistency between the input electric field amplitude and the output amplitude. The total electric field $E_\omega(\vec{r})$ at point \vec{r} can be represented as a superposition of all Bloch modes of the BPC [see Eq. (7)]. Inserting Eq. (7) into Eq. (8) and using Eq. (4), we obtain

$$\sum_{\vec{k},l} f_{\vec{k},l}(\omega_{\vec{k},l}^2 - \omega^2)\epsilon_b\psi_{\vec{k},l}(\vec{r}) = \omega^2 4\pi\chi_\omega(\vec{r})E_\omega(\vec{r}). \quad (9)$$

Multiplying both sides of Eq. (9) by $\psi_{\vec{q},n}^*(\vec{r})$, integrating over the whole photonic crystal, and using Eqs. (6a) and (6b), we obtain

$$f_{\vec{q},n} = \frac{1}{\mathcal{V}} \int_{\mathcal{V}} d^2r' \frac{\psi_{\vec{q},n}^*(\vec{r}')}{\Delta_{\vec{q},n}} 4\pi\chi_{\omega}(\vec{r}') E_{\omega}(\vec{r}'), \quad (10a)$$

where

$$\Delta_{\vec{q},n} \equiv \left(\frac{\omega_{\vec{q},n}^2}{\omega^2} - 1 \right) a_{\vec{q},n}. \quad (10b)$$

Multiplying both sides of Eq. (10a) by $\psi_{\vec{q},n}(\vec{r})$ and summing over $\{\vec{q},n\}$, we obtain the required integral equation

$$E_{\omega}(\vec{r}) = \frac{1}{\mathcal{V}} \int_{\mathcal{V}} d^2r' \hat{G}_{\omega}(\vec{r},\vec{r}') 4\pi\chi_{\omega}(\vec{r}') E_{\omega}(\vec{r}'), \quad (11)$$

where

$$\hat{G}_{\omega}(\vec{r},\vec{r}') = \sum_{\vec{q},l} \frac{\psi_{\vec{q},l}(\vec{r}) \psi_{\vec{q},l}^*(\vec{r}')}{\Delta_{\vec{q},l}} \quad (12)$$

is the Green's function of the BPC.

IV. PERIODIC INCLUSIONS WITHIN A METALLIC FILAMENT

We now specialize our treatment to perturbations of the BPC that preserve the periodicity of the metallic PC. In this case

$$\chi(\vec{r}) = \sum_{\vec{R}} \bar{\chi}(\vec{r} + \vec{R}), \quad (13)$$

where \vec{R} is a translation vector of the BPC and $\bar{\chi}(\vec{r})$ is a function different from zero only within the primitive cell of the BPC. We seek solutions $E_{\omega}(\vec{r})$ of Eq. (11) that satisfy the Bloch periodicity

$$E_{\omega}(\vec{r} + \vec{R}) = e^{i\vec{q}\cdot\vec{R}} E_{\omega}(\vec{r}), \quad (14)$$

where \vec{q} is a Bloch vector from the first Brillouin zone of the lattice. Using Eqs. (11), (13), and (14) we can write

$$E_{\omega}(\vec{r}) = \frac{1}{\mathcal{V}_0} \int_{\mathcal{V}_0} d^2r' \mathcal{G}_{\omega,\vec{q}}(\vec{r},\vec{r}') 4\pi\bar{\chi}(\vec{r}') E_{\omega}(\vec{r}'), \quad (15a)$$

where

$$\mathcal{G}_{\omega,\vec{q}}(\vec{r},\vec{r}') \equiv \sum_l \frac{\psi_{\vec{q},l}(\vec{r}) \psi_{\vec{q},l}^*(\vec{r}')}{\Delta_{\vec{q},l}}, \quad (15b)$$

and where $\mathcal{V}_0 = \mathcal{V}/N$ is the two-dimensional volume of the unit cell (defined in the plane of periodicity) of a PC with N unit cells, spanning a total volume \mathcal{V} . In the following we use the notation

$$\langle \psi_1 | \xi | \psi_2 \rangle \equiv \frac{1}{\mathcal{V}_0} \int_{\mathcal{V}_0} d^2r \psi_1^*(\vec{r}) \psi_2(\vec{r}) \xi(\vec{r}). \quad (16)$$

From Eqs. (15a), (15b), and (7), and the orthonormality given by Eqs. (6a) and (6b), we obtain an iterative equation for the expansion coefficients of the full Bloch wave amplitude:

$$f_{\vec{k}_2,l_2} = \delta_{\vec{q},\vec{k}_2} \frac{1}{\Delta_{\vec{q},l_2} \Delta_{\vec{q},l_2} \vec{k}_1,l_1} \sum \langle \psi_{\vec{q},l_2} | 4\pi\bar{\chi} | \psi_{\vec{k}_1,l_1} \rangle f_{\vec{k}_1,l_1}. \quad (17)$$

Equation (17) reveals that $f_{\vec{k}_2,l_2} = 0$ if $\vec{k}_2 \neq \vec{q}$, $\forall l_2$. Using this observation and introducing $h_{\vec{q},l} \equiv f_{\vec{q},l} \omega_{\vec{q},l} / c$, we obtain

$$\sum_{l_1} B_{\vec{q}}(l_2;l_1) h_{\vec{q},l_1} = \frac{c^2}{\omega^2} h_{\vec{q},l_2}, \quad (18a)$$

where

$$B_{\vec{q}}(l_2;l_1) \equiv \frac{\delta_{l_2,l_1}}{\omega_{\vec{q},l_2}^2 / c^2} + \frac{\langle \tilde{\psi}_{\vec{q},l_2} | 4\pi\bar{\chi} | \tilde{\psi}_{\vec{q},l_1} \rangle}{1 + (\omega_p^2 / c^2) \langle \tilde{\psi}_{\vec{q},l_2} | \theta_M | \tilde{\psi}_{\vec{q},l_2} \rangle} \quad (18b)$$

and [see the Appendix for the definition of $\psi_{\vec{k},l}(\vec{r})$]

$$\tilde{\psi}_{\vec{k},l}(\vec{r}) \equiv \frac{\psi_{\vec{k},l}(\vec{r})}{\omega_{\vec{q},l} / c} = \frac{e^{i\vec{k}\cdot\vec{r}} \sum_{\vec{G}} \tilde{u}_{\vec{k},l}(\vec{G}) e^{i\vec{G}\cdot\vec{r}}}{\vec{G}} \frac{1}{\sqrt{\sum_{\vec{G}} (\vec{k} + \vec{G})^2 |\tilde{u}_{\vec{k},l}(\vec{G})|^2}}. \quad (18c)$$

Equation (18a) can be rewritten in the form of a standard eigenvalue equation by multiplying both sides with the inverse matrix $B_{\vec{q}}^{-1}(l_3;l_2)$ and summing over l_2 :

$$\sum_{l_2} B_{\vec{q}}^{-1}(l_3;l_2) h_{\vec{q},l_2} = \frac{\omega^2}{c^2} h_{\vec{q},l_3}. \quad (19)$$

V. PHOTONIC BAND STRUCTURE OF A METALLIC FILAMENT WITHOUT LOSS

To verify the validity and numerical accuracy of our integral equation formulation for the negative dielectric function BPC, we consider a simple Drude model for metallic rods of radius $r=0.4a$ in a 2D square lattice, where a is the lattice constant. The dielectric function in the metal is modeled as $\epsilon_a(\omega) = \epsilon_0 - \omega_p^2 / \omega^2$, where the plasma frequency is chosen to be that of bulk silver. The metal rods are embedded in a matrix with dielectric constant ϵ_b . In this diagnostic calculation we neglect all imaginary parts of the dielectric functions. The scaled plasma frequency of the metal is $\omega_{ps} = a/\lambda_p$. For silver $1/\lambda_p = 7.27 \mu\text{m}^{-1}$, and $\epsilon_0 = 1.0$ [20]. We consider a PC with $\epsilon_b = 4.0$ and we choose the lattice constant $a = 320 \text{ nm} \Rightarrow \omega_{ps} = 2.33$. The total dielectric function of the photonic crystal, Eq. (5), can be separated into two equivalent forms:

$$(i) \quad \epsilon_{\text{BPC}}(\vec{r}) = \epsilon_b - (\omega_p^2 / \omega^2) \theta_M(\vec{r})$$

and

$$4\pi\chi_{\omega}(\vec{r}) = (\epsilon_0 - \epsilon_b) \theta_M(\vec{r});$$

$$(ii) \quad \epsilon_{\text{BPC}}(\vec{r}) = \epsilon_0 - (\omega_p^2 / \omega^2) \theta_M(\vec{r})$$

and

$$4\pi\chi_{\omega}(\vec{r}) = (\epsilon_b - \epsilon_0) [1 - \theta_M(\vec{r})].$$

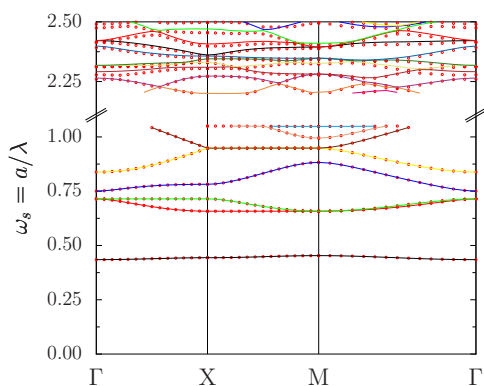


FIG. 1. (Color online) Comparison of photonic band structure obtained by CSM and integral equation method for a 2D square lattice of metallic rods with $r=0.4a$ and $\epsilon_a = \epsilon_0 - \omega_{ps}^2/\omega_s^2$, where $\epsilon_0 = 1.0$ and $\omega_{ps} = 2.33$, in dielectric background of $\epsilon_b = 4.0$. Solid lines represent the photonic band structure obtained by our self-consistent, iterative method. 3000 plane waves are used to calculate the BPC band structure and only the first 150 BPC modes are considered coupled from the perturbation. The dots represent the calculation using the CSM. The agreement is nearly perfect for the eight lowest bands but deteriorating for higher bands due to the limited number of BPC modes used in constructing the Bloch modes of the complete PC.

These two partitions differ (assuming $\epsilon_0 \neq \epsilon_b$) in the set of BPC basis functions used to represent the total electric field Eq. (7). The perturbation $4\pi\chi_\omega(\vec{r})$ in case (i) is uniformly distributed within metallic rods [$\sim\theta_M(\vec{r})$], whereas in case (ii) it is uniformly distributed outside the metal [$\sim[1 - \theta_M(\vec{r})]$]. We compare the numerically determined photonic band structure of these two formulations of the same problem with the previously established cutting surface method [15] as a consistency check of the formulation Eq. (19). 3000 plane waves are used to determine the eigenfunctions of the BPC, and only the first 150 BPC modes are considered in constructing the Bloch modes of the complete PC. We have verified that the results of cases (i) and (ii) are identical as expected. In addition, we use the CSM with 3000 plane waves for each of 200 pairs [$\epsilon_a, \epsilon_b = 4.0$] where ϵ_a is varied in the range $(-40, 5)$. The cutting surface is determined from the equation $\epsilon_a = 1.0 - \omega_{ps}^2/\omega_s^2$. The results of our self-consistent integral equation and the CSM are shown in Fig. 1. For lower bands, the agreement between the CSM and our integral equation approach is nearly perfect.

VI. INCLUSION OF INHOMOGENEOUSLY BROADENED NONLINEAR RESONATORS

We now apply our computational method to explore the possibility of nonlinear Bloch waves with purely real eigenfrequency in lossy metallic filaments where complex dielectric functions are obtained from experimental data. As a possible counterbalance to intrinsic losses in realistic metals, we include nonlinear resonators that are activated by external incoherent pumping within the void regions of the filament. We also consider a thin layer of strong resonators on the interior surfaces of the periodically structured metal filament

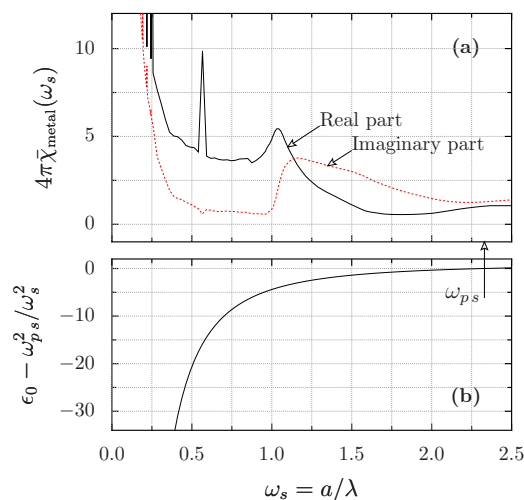


FIG. 2. (Color online) Full dielectric function of silver determined experimentally at room temperature is $\epsilon(\omega) = \epsilon_0 - \omega_p^2/\omega^2 + 4\pi\bar{\chi}_{\text{metal}}(\omega)$. The lattice constant $a=320$ nm is used to calculate the scaled frequencies $\omega_s = a/\lambda$. (a) The remaining optical dielectric function $4\pi\bar{\chi}_{\text{metal}}(\omega_s)$, after (b) the real Drude part $\epsilon_0 - \omega_{ps}^2/\omega_s^2$, where $\epsilon_0 = 1.0$ and $\omega_{ps} = 2.33$, is subtracted from the full dielectric function. Spectral features observed in $\bar{\chi}_{\text{metal}}(\omega_s)$ are related to electronic interband transitions in bulk silver.

that may be activated by an electrical current.

These resonators can provide additional loss when residing in their ground state but can also provide gain to the PC filament when pumped to their excited state. We find, remarkably, that in spite of significant absorption losses, nonlinear Bloch waves can be excited within the optical pass band of the metallic PC at frequencies below the effective plasma cutoff frequency [see [13], Eq. (2.6), in which $\omega_{ps, \text{eff}} \approx \omega_{ps}\sqrt{f}$, where f is the metallic filling fraction of the unit cell]. These nonlinear Bloch waves exhibit a laserlike input-output characteristic and propagate primarily through the nonmetallic void regions of the PC filament. We consider a square lattice ($a=320$ nm) of cylindrical silver rods with radius $r=0.4a$ situated in air. The effective plasma cutoff frequency for this PC is $\omega_{ps, \text{eff}} = \omega_{ps}0.4\sqrt{\pi} \approx 1.7$. The full dielectric function of silver is $\epsilon_a(\omega) = \epsilon_0 - \omega_p^2/\omega^2 + 4\pi\bar{\chi}_{\text{metal}}(\omega)$ where $\epsilon_0 = 1.0$, $\omega_p/2\pi = 1/\lambda_p = 7.27 \mu\text{m}^{-1}$, and $\bar{\chi}_{\text{metal}}(\omega)$ is taken from optical measurement of the silver dielectric function at room temperature [20]. Experimental data used to define $\bar{\chi}_{\text{metal}}(\omega)$ are shown in Fig. 2. The real and imaginary parts of $4\pi\bar{\chi}_{\text{metal}}(\omega)$ are drawn in Fig. 2(a), while the Drude-type backbone dielectric function is depicted in Fig. 2(b).

We consider three situations of experimental relevance: (a) the air regions of the above-described metallic PC are completely filled with a close-packed array of suitably capped colloidal quantum dots, (b) a thin layer of random surface resonators (of thickness $\sim 0.04a$) is present around each and every silver rod and the remaining void regions consist of air, and (c) a thin layer of random surface resonators (of thickness 48 nm) surrounds each tungsten rod. We assume that the dielectric function of the resonators has a constant part, 4.0 in each case, as well as a frequency-dependent part modeled as an inhomogeneously broadened

collection of two-level systems. Each individual quantum two-level system is attributed a transition frequency ω_{0s} and homogeneously broadened susceptibility

$$\bar{\chi}_{\text{res}}(\vec{r}, \omega_s; \omega_{0s}) = g_0 \frac{(\omega_s - \omega_{0s})\tau_2 - i}{1 + (\omega_s - \omega_{0s})^2\tau_2^2 + I_{\omega_s}(\vec{r})\omega_s\omega_{0s}^{-1}}. \quad (20)$$

The factor $g_0 = (d^2 a \tau_2 / 2 \pi \hbar c \epsilon_0)[(\rho - 1)/(\rho + 1)]N_T$ [21] is proportional to the concentration of the quantum dots or other resonators per unit volume, N_T , and to the square of the transition electric dipole moment d . The sign of g_0 (gain or loss) depends on the pump parameter ρ . For realistic quantum dots such as 5-nm-diameter PbS nanocrystals, the parameters of Eq. (20) are $d \sim 2 \times 10^{-29}$ C m ≈ 6 D (where by definition one debye is $1 \text{ D} = 3.336 \times 10^{-30}$ C m) [22,23] and assuming a (reasonable) dephasing time $T_2 \approx 1$ ps, we obtain $\tau_2 \approx 5.1 \times 10^3$. For a close-packed collection of quantum dots of diameter 5 nm and capping layer of thickness 2 nm we set $N_T \sim 10^{18} \text{ cm}^{-3}$.

$$I_{\omega_s}(\vec{r}) \sim n_{\text{ph}}[(1.76 \times 10^{-2})/\omega_{0s}^3(\rho + 1)]|\psi_{\vec{q}}(\vec{r})|^2$$

where $n_{\text{ph}} = b \int_{\mathcal{V}_0} d^2 r \overline{U_E(\vec{r}, t)} / \hbar \omega_R$ is the number of photons per unit cell $\mathcal{V}_0 b$ (\mathcal{V}_0 is the two-dimensional volume, b is the hypothetical height of the cell, and n_{ph} is defined as the ratio of the average energy in the electromagnetic field of frequency ω_R to the energy of a photon with the same frequency) [19]. $|\psi_{\vec{q}}(\vec{r})|^2 = |\sum_i f_{\vec{q},i} \psi_{\vec{q},i}(\vec{r})|^2$ is the normalized, nonlinear, Bloch mode field modulus squared, and the normalization condition is given by [19]

$$\frac{1}{\mathcal{V}_0} \int_{\mathcal{V}_0} d^2 r \psi_{\vec{q}}^*(\vec{r}) \frac{\partial [\omega \epsilon_R(\omega)]}{\partial \omega} \Big|_{\omega_R} \psi_{\vec{q}}(\vec{r}) \equiv 1. \quad (21)$$

Further details of this quantum dot model are found in Ref. [19], Appendix D. We assume that the resonance frequencies ω_{0s} of individual quantum dots are uniformly distributed over an interval of frequencies $\Delta\omega_s$ around a central frequency $\bar{\omega}_{0s}$. In accord with typical PbS quantum dot size distributions, we take $\Delta\omega_s \approx 5\% \times \bar{\omega}_{0s}$ [24]. The average complex susceptibility of the inhomogeneously broadened collection of quantum dots is given by

$$\bar{\chi}_{\text{inh}}(\vec{r}, \omega_s) = \int_{\bar{\omega}_{0s} - \Delta\omega_s/2}^{\bar{\omega}_{0s} + \Delta\omega_s/2} \frac{1}{\Delta\omega_s} d\omega_{0s} \bar{\chi}_{\text{res}}(\vec{r}, \omega_s; \omega_{0s}). \quad (22)$$

Figure 3(a) depicts the inhomogeneously broadened susceptibility of the collection of the quantum dots obtained by numerically evaluating Eq. (22) using the homogeneously broadened susceptibility Eq. (20) with $I_{\omega_s}(\vec{r}) \equiv 0$ [drawn in Fig. 3(b)]. The real and imaginary parts of the susceptibilities drawn in Fig. 3 are normalized to 1 for ease of presentation.

A. Photonic crystal filament fully infiltrated with inhomogeneously broadened colloidal quantum dots

We first consider the silver PC filament, described above, to be fully infiltrated with inhomogeneously broadened, close-packed quantum dots, as schematically shown in Fig.

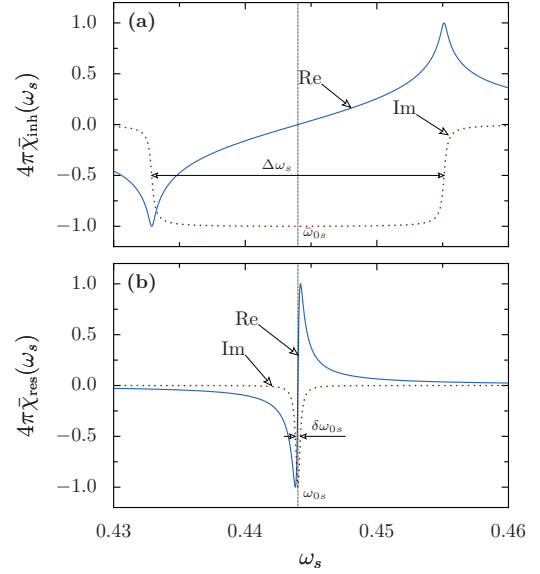


FIG. 3. (Color online) (a) Inhomogeneously broadened susceptibility of the collection of quantum dots with resonance frequencies uniformly distributed in the scaled frequency interval $\Delta\omega_s$ around $\bar{\omega}_{0s}$. (b) Homogeneously broadened susceptibility of the quantum dots with resonance frequency ω_{0s} . In both graphs the real part of the susceptibility is drawn with a solid (blue) line and the imaginary part with a dotted (brown) line. All curves are scaled to unit maximum amplitude for convenience.

4(a). The average (frequency-independent) dielectric constant of the quantum dots is $\epsilon_b = 4.0$. The dielectric function of the region occupied by quantum dots is $\epsilon_b + 4\pi\bar{\chi}_{\text{inh}}$, where the inhomogeneously broadened susceptibility $\bar{\chi}_{\text{inh}}$ is given by Eq. (22). The BPC photonic band structure of the Drude-type metallic rods ($r = 0.4a$, $\epsilon_0 = 1.0$, $\omega_{ps} = 2.33$) in constant dielectric background ($\epsilon_b = 4.0$) is shown in Fig. 5. The optical pass band (first photonic band) within the PBG spans a scaled frequency range of ~ 0.0186 , starting from $\omega_s = 0.4347$ at the Γ point and ending with $\omega_s = 0.4533$ at the M point of the first Brillouin zone.

We choose the central frequency $\bar{\omega}_{0s}$ of the distribution of the quantum dots at a scaled frequency $\omega_s = 0.4440$ in coincidence with the mid-frequency of the optical pass band. Given the 5% inhomogeneous broadening, the frequency dis-

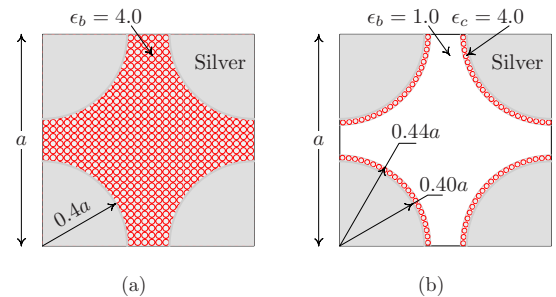


FIG. 4. (Color online) (a) Unit cell of metallic photonic crystal where the void regions between silver cylindrical rods of radius $r = 0.4a$ are infiltrated with close-packed quantum dots. (b) The same metallic PC as in (a) but now only a thin layer of random surface resonators is covering all interior surfaces.

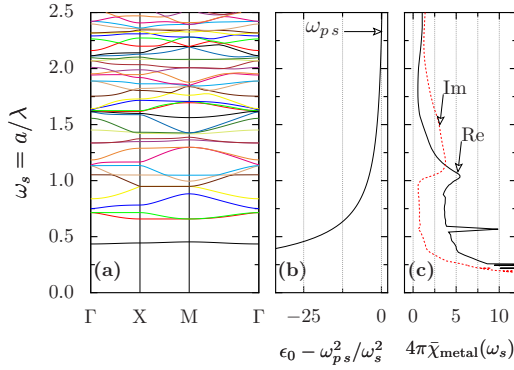


FIG. 5. (Color online) Frequency correspondence between photonic band structure and metallic dielectric function. Band structure shown in (a) is obtained by using the Drude-type dielectric function drawn in (b). (c) shows the “residue” dielectric function of silver used as part of the final “perturbation” $4\pi\bar{\chi}$.

tribution of the quantum dots spans a frequency range of $\Delta\omega_s=0.0222$, affording gain to the whole pass band.

When we include the non-Drude portion of the dielectric function of the silver rods $\bar{\chi}_{\text{metal}}(\omega_s)$, the overall perturbation of the backbone photonic crystal (Drude model metallic rods with dielectric function $\epsilon_0 - \omega_{ps}^2/\omega_s^2$, $\epsilon_0=1.0$, $\omega_{ps}=2.33$, in dielectric constant $\epsilon_b=4.0$ background) becomes

$$\bar{\chi} = \left(\frac{\epsilon_b - \epsilon_0}{4\pi} + \bar{\chi}_{\text{inh}}(\vec{r}, \omega_s) \right) [1 - \theta_M(\vec{r})] + \bar{\chi}_{\text{metal}}(\omega_s) \theta_M(\vec{r}). \quad (23)$$

As a preliminary exercise to solving the full problem, we replace the inhomogeneously broadened susceptibility of the quantum dots with a position- and frequency-independent, real parameter, namely, $4\pi\bar{\chi}_{\text{inh}}(\vec{r}, \omega_s) = \text{const}$. We substitute this constant value in Eq. (23), and then insert only the real part of Eq. (23) into Eq. (19). Since the real part of Eq. (23) depends on the scaled frequency through $\bar{\chi}_{\text{metal}}$, we solve Eq. (19) self-consistently. $\bar{\chi}_{\text{metal}}(\omega_s)$ is taken from the experiment. An interpolation procedure for finding $\bar{\chi}_{\text{metal}}$ values for any desired scaled frequency based on the discrete data from the optical measurement of the silver dielectric function is used.

This preliminary process enables us to observe how the frequencies of the photonic pass band, for different Bloch vectors, depend on specific (hypothetical) constant values of $\bar{\chi}_{\text{inh}}$. We self-consistently calculate the frequencies of the first photonic pass band for the Γ , X , and M points, for the constant in the range $(-0.3, 0.3)$, and draw the results in Fig. 6. In reality, the constant depends on the scaled frequency via $\bar{\chi}_{\text{inh}}(\omega_s)$. We draw the real part of $\bar{\chi}_{\text{inh}}(\omega_s)$ in Fig. 6 for comparison with the Γ , X , and M trajectories.

From Fig. 6 we observe that the $4\pi\bar{\chi}_{\text{inh}}=0$ (horizontal) line intersects the Γ - and M -point trajectories at lower frequencies than 0.4347 and 0.4533 (the Drude BPC), respectively. These intersections represent the band edges of the first pass band for the “augmented” BPC, with the real part of the leftover (non-Drude) susceptibility of silver rods taken into account.

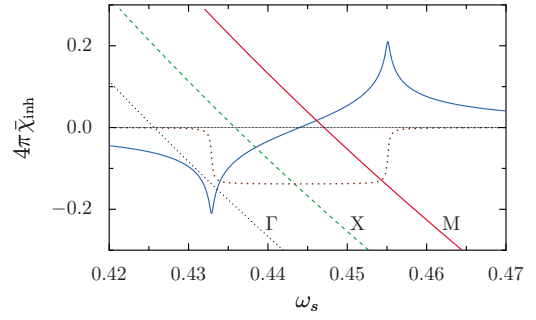


FIG. 6. (Color online) Real (solid blue) and imaginary (dashed brown) parts of the inhomogeneously broadened susceptibility of the collection of quantum dots with resonance frequencies uniformly distributed in the scaled frequency interval $\Delta\omega_s=0.0222$ around $\bar{\omega}_{0s}=0.444$, for $\rho=\infty$. Three additional lines represent the trajectory of the frequencies of the first band for the M (solid red line), X (dashed green line), and Γ (dotted black line) points as the value of $4\pi\bar{\chi}_{\text{inh}}=\text{const}$ is varied.

If the frequency dependence of $\bar{\chi}_{\text{inh}}$ is considered, an additional self-consistent calculation of Eq. (19) is needed. Results of this self-consistent calculation may be inferred from Fig. 6. For illustration, consider the point in the graph where the X -point trajectory intersects the $4\pi\bar{\chi}_{\text{inh}}=0$ line. The abscissa of the intersection point, ω_{s0} , is the X -point frequency of the first photonic pass band when the inhomogeneously broadened resonators are switched off. Plugging ω_{s0} into $4\pi\bar{\chi}_{\text{inh}}(\omega_s)$ yields the initial value of $\text{const}=4\pi\bar{\chi}_{\text{inh}}(\omega_{s0})$. We then find the intersection of the X -point trajectory with the horizontal line passing through this value of the constant. The abscissa of this intersection determines the updated X -point frequency ω_{s1} of the first photonic pass band. We use ω_{s1} to obtain the updated value of the constant given by $4\pi\bar{\chi}_{\text{inh}}(\omega_{s1})$, and so forth. The convergence of this calculation depends on the relative slope of the X -point trajectory and the $4\pi\bar{\chi}_{\text{inh}}$ curve. From Fig. 6, we conclude that the convergence of the calculation for the M and X points is expected, but this is less obvious for the Γ point. The iterative procedure is described in more detail in [19]. In our actual calculations we consider the frequency dependence of $\bar{\chi}_{\text{inh}}$ and $\bar{\chi}_{\text{metal}}$ simultaneously and do not separate the self-consistent procedure into the two steps described above. Furthermore, we include the imaginary parts of both $\bar{\chi}_{\text{metal}}$ and $\bar{\chi}_{\text{inh}}$. This leads to the laserlike transition in the photon number per unit cell, n_{ph} , versus pump ρ as shown in Fig. 7. By using the complex $\bar{\chi}_{\text{metal}}(\omega_s)$ (over and above the Drude model), we realistically model a metallic PC where losses incurred by electromagnetic waves in the metallic regions are accounted for. The rod radius is chosen as $r=0.4a$ for two reasons: (i) to place the first photonic pass band in a frequency region where metallic losses are minimized, and (ii) to avoid a sharp spectral feature of $\bar{\chi}_{\text{metal}}(\omega_s)$ at $\omega_s \approx 0.55$ arising from electronic interband transitions in bulk silver.

From Fig. 7 we observe that, in contrast with pure homogeneous broadening [19], the frequency of the nonlinear Bloch wave for inhomogeneously broadened resonators does not clamp to a single value but varies monotonically with the pump parameter. This may be attributed to the wandering of the mode toward other frequencies where gain is not yet used (different sets of resonators).

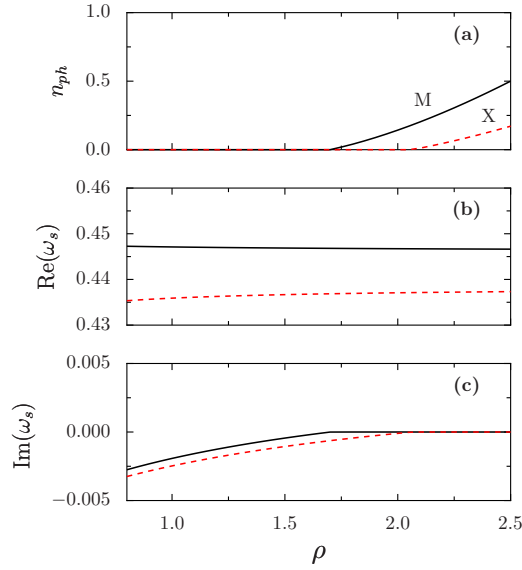


FIG. 7. (Color online) Shown as a function of the pump parameter ρ are (a) the number of photons per unit cell, n_{ph} , in the self-consistent nonlinear Bloch wave, (b) the real part of the Bloch wave frequency, and (c) the imaginary part of the Bloch wave frequency for the first photonic band at the M point (solid black lines) and at the X point (dashed red lines).

B. Photonic crystal filament with random surface resonators

For PC filaments with rough metal surfaces, we consider two different situations. In the first model, the metallic rods are described by the dielectric function of silver measured at room temperature. In the second model, the dielectric response of the rods is described by a Drude function where the parameters (plasma frequency and electron mean collision time) for tungsten are used. In addition, the electron mean collision time is modeled as depending inversely on the absolute temperature, and the high-temperature behavior of a microstructured tungsten filament is inferred.

1. Microstructured silver filament at room temperature

As in the previous section, we consider a square lattice of cylindrical silver rods with radius $r=0.4a$ (where $a=0.32 \mu\text{m}$ is the lattice constant) in air. Now the interior metal surfaces of the PC are assumed to be covered with a thin layer of inhomogeneously broadened resonators, as is schematically shown in Fig. 4(b). The thickness of the resonator layer is $\sim 0.04a \approx 13 \text{ nm}$. The average (frequency-independent part) dielectric constant of the resonator layer is, again, $\epsilon_c=4.0$. The dielectric function of the region occupied by the resonators is $\epsilon_c + 4\pi\bar{\chi}_{inh}$, where the inhomogeneously broadened susceptibility $\bar{\chi}_{inh}$ is given by Eq. (22). The photonic band structure of a PC with Drude metallic rods, coated with the thin dielectric layer of $\epsilon_c=4.0$ and situated in air $\epsilon_b=1.0$, is shown in Fig. 8. The isolated optical pass band (below the effective plasma frequency) of the filament spans a scaled frequency range of ~ 0.0532 , starting from $\omega_s=0.7788$ at the Γ point and ending with $\omega_s=0.8320$ at the M point of the first Brillouin zone [see Fig. 8(a)]. An illustration for the magnitudes of the electric field of the Bloch modes at

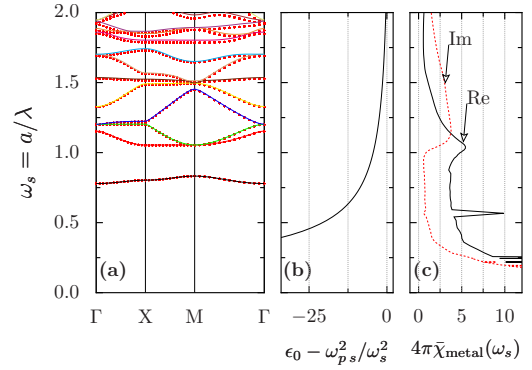


FIG. 8. (Color online) Photonic band structure for the 2D silver backbone photonic crystal with unit cell depicted in Fig. 4(b). (a) is obtained using the Drude-type dielectric function for the metallic rods [shown in (b)]. Photonic band structure calculated using our self-consistent integral equation (solid lines) is compared with results of CSM (red dots). (c) shows the residue dielectric function of silver used as part of the final perturbation $4\pi\bar{\chi}$. Rods are coated with a quantum dot layer of thickness $0.04a$. Quantum dots have a volumetric concentration $N_T=10^{18} \text{ cm}^{-3}$ and the same electric dipole moment d (d is varied in the range 18–30 D).

X and M points of this band is given in Fig. 9.

The transition frequencies of resonators are chosen to be uniformly distributed in the interval of scaled frequencies (0.741,0.789), corresponding to 6% inhomogeneous broadening and covering the spectral range of the optical pass band. When we include the non-Drude portion of the dielectric function of the silver rods, $\bar{\chi}_{metal}(\omega_s)$, the overall perturbation of the backbone photonic crystal becomes

$$\bar{\chi} = \left(\frac{\epsilon_c - \epsilon_b}{4\pi} + \bar{\chi}_{inh}(\vec{r}, \omega_s) \right) \theta_C(\vec{r}) + \bar{\chi}_{metal}(\omega_s) \theta_M(\vec{r}), \quad (24a)$$

where $\theta_M(\vec{r})$ is defined in Eq. (2), and

$$\theta_C(\vec{r}) = \begin{cases} 1 & \text{in thin coating region,} \\ 0 & \text{otherwise.} \end{cases} \quad (24b)$$

Using the same iteration procedure as described in the previous section, we observe that the lasinglike transition in

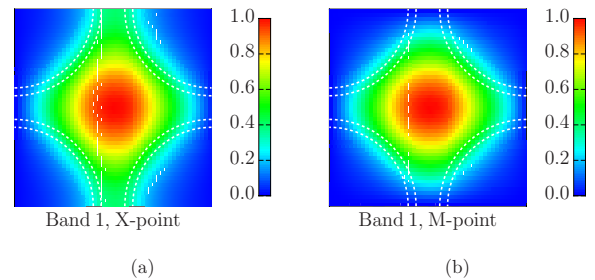


FIG. 9. (Color online) Absolute value of the electric field of Bloch modes in the first photonic band at (a) X and (b) M points with no losses (or gain) present. Clearly, the optical pass band supports light that propagates primarily through the void regions of the filament with only evanescent coupling into metal rods.

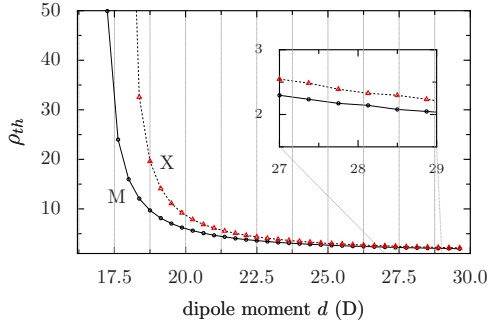


FIG. 10. (Color online) Pump threshold ρ_{th} for the laserlike transition as a function of the dipole moment d ($1 \text{ D} = 3.336 \times 10^{-30} \text{ C m}$) of quantum dots (volumetric density $N_T \sim 10^{18} \text{ cm}^{-3}$), forming a thin coating around silver rods. Stronger pumping is needed to support nonlinear Bloch waves at the X point (dashed line, triangular red dots) than at the M point (solid line, circular black dots) for the same dipole moment and density of quantum dots.

the photon number per unit cell, n_{ph} , is not possible if the volumetric density of quantum dots, N_T , and their dipole moment d are the same ($N_T \sim 10^{18} \text{ cm}^{-3}$ and $d \sim 6 \text{ D}$) as used for the colloidal quantum dots of the previous section. This is understandable since the gain provided by the thin surface layer is not sufficient to overcome losses incurred by that part of electric field penetrating the metallic region. Given the size of localized surface plasmon resonators [16,17,25], we once again choose to keep $N_T = 10^{18} \text{ cm}^{-3}$ and vary the dipole moment of quantum dots. We scan a range of dipole moments from three to five times the colloidal quantum dot value ($d \approx 6 \text{ D}$) used previously. These high values for the dipole moments may be difficult to achieve using single-electron interband transitions in quantum dots. However, they may be possible for other resonance mechanisms (e.g., electronic excitation of localized plasmons in granular material [25]) associated with a rough metal surface. In metals deposited by sputtering techniques [17], surface roughness is responsible for the occurrence of localized surface plasmon resonances (LSPs) excited by either an external electromagnetic field or the propagation of a nearby extended surface plasmon [16]. LSP resonances exhibit a frequency distribution compatible with the size randomness of the metallic grains on the silver film. Therefore they can be modeled as an inhomogeneously broadened collection of surface resonators. Similar to the excitation by the extended surface plasmon, localized surface plasmon resonances may also be excited by an electrical current injected through the interior of the metal.

The dependence of the pump threshold for the laserlike transition as a function of the dipole moment d is shown in Fig. 10. Roughly speaking, a dipole moment of at least 18 D is necessary for the emergence of the nonlinear Bloch modes, given our assumed losses in the metal. This required dipole strength decreases continuously as the thickness of the surface roughening layer is increased.

2. Hot microstructured tungsten filament

We consider a square lattice ($a = 2.8 \mu\text{m}$) of cylindrical tungsten rods with radius $r = 0.4a$ in air background analo-

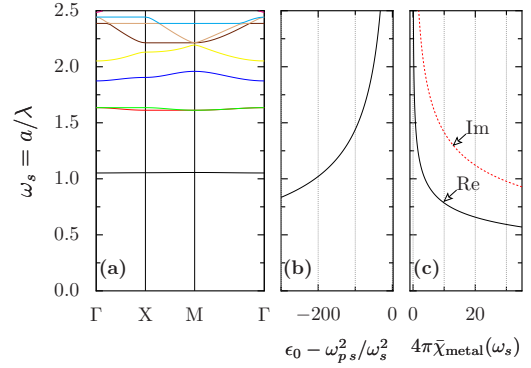


FIG. 11. (Color online) Photonic band structure for the 2D tungsten backbone photonic crystal with unit cell similar to Fig. 4(b) (now the coating has a thickness $0.017a$). (a) is obtained by using a Drude-type dielectric function for the metallic rods [drawn in (b)]. Photonic band structure is calculated using our self-consistent integral equation (solid lines) and compared to the CSM results (red dots). (c) shows the residue dielectric function of tungsten used as part of the final perturbation $4\pi\bar{\chi}_{\text{metal}}$.

gous to the 3D woodpile photonic crystal used in measurements of anomalous blackbody radiation [11]. The full dielectric function of tungsten is

$$\epsilon_a(\omega_s) = \epsilon_0 - \omega_{ps}^2/\omega_s^2 + 4\pi\bar{\chi}_{\text{metal}}(\omega_s)$$

where

$$\epsilon_0 = 1.0,$$

$$\omega_{ps} = a/\lambda_p = 2.8 \mu\text{m} \times 5.17 \mu\text{m}^{-1} = 14.476.$$

The Drude modeled dielectric response of the metal is given by

$$4\pi\bar{\chi}_{\text{metal}}(\omega_s) = \frac{\omega_{ps}^2}{\omega_s^2(1 + \omega_s^2\tau^2)} + i\frac{\omega_{ps}^2\tau}{\omega_s(1 + \omega_s^2\tau^2)}, \quad (25)$$

where $\tau = (T_0/T)\tau_0$, $T_0 = 290 \text{ K}$, and $\tau_0 = \lambda_\tau/a = 1/(2.8 \mu\text{m} \times 4.87 \times 10^{-2} \mu\text{m}^{-1}) = 7.334$ [26–28]. Our choice for the temperature dependence of τ is consistent with the linear temperature of the resistivity of metals at temperatures large compared to the metallic phonon Debye frequency [29].

The photonic band structure of the backbone photonic crystal is shown in Fig. 11(a). The first photonic band is very flat, starting from $\omega_s = 1.052$ at the Γ point and ending with $\omega_s = 1.056$ at the M point of the first Brillouin zone. The mean frequency of the first photonic band corresponds to a wavelength $\lambda \approx 2.7 \mu\text{m}$. The room temperature “perturbation” $4\pi\bar{\chi}_{\text{metal}}(\omega_s)$ is depicted in Fig. 11(c). The dependence of $4\pi\bar{\chi}_{\text{metal}}(\omega_s)$ on the temperature is shown in Fig. 12. For a temperature of about 2290 K, the real part of the perturbation reaches a value of around 100 [Fig. 12(b)] at a scaled frequency $\omega_s \approx 1$ [first photonic band of the BPC, Fig. 11(a)]. This perturbation value is large compared to the BPC dielectric function $\epsilon_0 - \omega_{ps}^2/\omega_s^2 = -200$ for the same scaled frequency $\omega_s \approx 1$ [Figs. 11(b) and 12(a)]. For even higher temperatures, the real part of the perturbation tends to cancel $-\omega_{ps}^2/\omega_s^2$ of the BPC dielectric function as is evident from

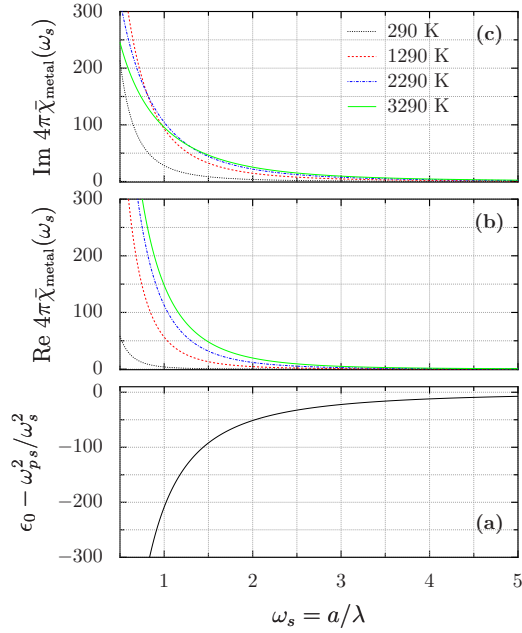


FIG. 12. (Color online) Drude dielectric response of tungsten for various temperatures where mean collision time of free electrons is modeled as varying inversely with temperature. Parameters used are $\omega_{ps}=14.476$, $\tau=(T_0/T)\tau_0$, $T_0=290$ K, and $\tau_0=7.334$ [26–28].

Eq. (25) using $\omega_s\tau \rightarrow 0$. Consequently, more BPC modes are needed to have an accurate computation of the frequency of the self-consistent nonlinear Bloch modes at high temperatures. Nevertheless, for a temperature of about 2290 K, using only the first 150 modes of the BPC and neglecting the imaginary part of the perturbation, we obtain a band structure to within 1% of that obtained by the CSM method. The imaginary part of the perturbation [Fig. 12(c)] initially increases with the temperature but decreases at higher temperatures.

We now coat the interior surfaces of the tungsten PC filament with an inhomogeneously broadened resonator layer of thickness $0.017a=48$ nm as shown in Fig. 3(b). The average (frequency-independent part) dielectric constant of the resonator layer is, again, $\epsilon_c=4.0$. The transition frequencies of resonators are chosen to be uniformly distributed in the interval of scaled frequencies (1.04,1.07), corresponding to 3% inhomogeneous broadening and covering the spectral range of the optical pass band. For a close-packed collection of resonators of diameter 5 nm separated from each other by a distance of 4 nm, we set $N_T=10^{18}$ cm $^{-3}$. Assuming a dephasing time $T_2 \approx 1$ ps for the resonators, we obtain $\tau_2 \approx 673.2$. All resonators are considered to have the same dipole moment. For illustration, we consider a series of values for the surface resonator dipole moment: $d \approx 17, 20, 22, 24$, and 30 D. We calculate the dependence of the threshold ρ_{th} for nonlinear Bloch waves on the temperature. Results are computed for only the M point in the reduced Brillouin zone and are shown in Fig. 13. We observe that for dipole moments below about 20 D, there is a critical temperature above which nonlinear Bloch modes do not emerge regardless of the pump ρ . Above the critical temperature, the gain provided by the

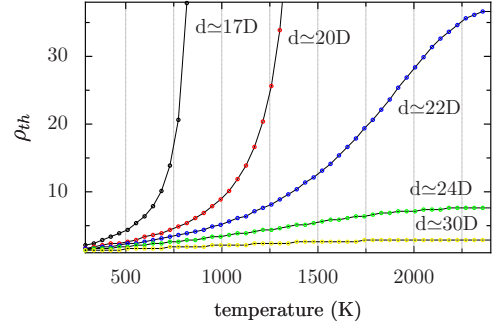


FIG. 13. (Color online) Temperature dependence of the threshold pump (for the emergence of nonlinear Bloch waves at the M point of the first electromagnetic band) for different magnitudes of the electric dipole moment of the surface resonators.

pumped resonators is insufficient to overcome the losses due to electronic scattering in the metallic regions. In contrast, for stronger resonances the pump threshold for exciting nonlinear Bloch waves shows a saturation with the temperature. This is a consequence of the Drude model for the imaginary part of the perturbation [Fig. 12(c)] which reaches its maximum value when $\omega_s\tau=1$ and then decreases with increasing temperature (smaller τ).

The persistence of nonlinear Bloch modes at high temperature in a metallic PBG filament may have striking consequences on the experimentally observed radiation spectrum [9–11]. When a current is driven through a connected 3D PBG filament, it may (i) excite phonons in the metal (leading to the measured temperature of the metal) and (ii) excite localized surface plasmon resonances in the metal (leading to an anomaly in the radiation spectrum mediated by nonlinear Bloch waves). As a result, strong peaks in the radiation spectrum may appear, over and above the conventional blackbody spectrum. The strength of radiation peaks caused by nonlinear Bloch waves would exhibit a nonlinear threshold behavior with pumping current.

VII. DISCUSSION

In this paper, we have demonstrated the emergence of nonlinear Bloch waves (waves that satisfy the Bloch periodicity, with purely real frequency and definite amplitude) in metallic PC filaments at frequencies below the effective plasma cutoff, under incoherent pumping. We have delineated detailed characteristics of these modes for two simple models: (i) a model of colloidal quantum dots infiltrated through the void regions of the 2D PC, and (ii) a model of a thin layer of resonators coating the inner surfaces of the metallic PC. Both quantum dots and surface resonators are modeled as two-level systems that can be inverted by incoherent pumping. Electromagnetic waves suffer losses while penetrating the resistive metallic rods. Experimental data are used to characterize the complex, frequency-dependent dielectric response of the metal to the electromagnetic field. Below a threshold pumping level, determined by the losses in the system, there are only transient extended electromagnetic modes in the metallic PC filament. Above the pumping

threshold, nonlinear Bloch waves emerge, with features similar to those of Bloch modes in a linear, lossless, photonic crystal. These nonlinear Bloch waves are particularly prominent when an isolated optical pass band appears below the effective plasma cutoff frequency of the metal. Unlike linear Bloch modes, the nonlinear Bloch waves are characterized by a definite amplitude (number of photons per unit cell) for each choice of the pump parameter. This nonlinear wave amplitude exhibits a laserlike input (pump)–output characteristic. This suggests that losses in photonic crystals may be offset by introducing regions of gain to yield propagating as well as stationary Bloch waves throughout the photonic crystal. Although our calculations were performed for 2D systems, similar optical pass bands and nonlinear Bloch waves are expected to arise in suitably structured 3D metallic PCs [30].

This work is an important generalization of the self-consistent nonlinear Bloch wave method used previously [19] to treat photonic crystals with purely positive real parts of their dielectric functions. Focusing of nonlinear Bloch waves to specific regions of the crystal is stronger in metallic PCs than in dielectric photonic crystals. Stronger focusing of light provides higher intensities and therefore higher interaction rates of the electromagnetic radiation with the resonators. In the present work, we considered an inhomogeneously broadened collection of resonators. We observe that distribution of gain over a broader region of frequencies, together with higher optical losses (despite the small penetration depth of radiation into metallic regions), is responsible for a higher pump threshold. In contrast to the case of purely homogeneous broadening, the nonlinear Bloch mode frequency does not clamp to a single value above the threshold pump.

In order to make more precise contact with thermal light emission experiments in periodically structured filaments [9–11], it is necessary to include several other factors in our model. Interaction between multiple nonlinear Bloch waves and competition for gain among these modes must be considered. It is also important to consider the finite size of the metallic PC filament and the nature (or lack thereof) of the thermodynamic equilibrium between nonlinear Bloch modes in the interior of the filament and exterior electromagnetic waves that are radiated into free space by the filament. This can change considerably for different boundary conditions, depending on whether the filament is fully or partially enclosed in an isothermal container or whether it radiates into free space. For practical application to enhanced light emission in the visible spectrum, it is useful to consider other metals such as iridium that have a much higher melting point than silver but have a much higher plasma frequency than tungsten. Finally, it is necessary to develop an appropriate electrical pumping model that defines the excitation of resonators within the structured metallic PBG filament. Nevertheless, our demonstration of nonlinear Bloch waves in periodically structured hot (high-resistivity), metallic filaments clearly suggests the possibility of anomalous light emission over and above the conventional blackbody spectrum, under strong pumping conditions.

ACKNOWLEDGMENTS

This work was supported in part by the Natural Sciences and Engineering Research Council of Canada, the Canadian Institute for Advanced Research, and the Ontario Premier's Platinum Research Fund.

APPENDIX: NORMALIZATION OF EIGENMODES FOR THE BACKBONE PHOTONIC CRYSTAL

Here we describe in detail the linear matrix equation for Bloch modes in the backbone photonic crystal consisting of Drude metal in a *real*, *positive*, and *constant* dielectric background. We derive the normalization parameter $\alpha_{\vec{k},l}$ for a Bloch mode of the BPC with Bloch wave vector \vec{k} and band index l .

Since the step function $\theta(\vec{r})$, introduced in Eq. (2), has the periodicity of the BPC, it can be Fourier decomposed in the reciprocal lattice. We write $\theta(\vec{r}) = \sum_{\vec{G}} \tilde{\theta}_{\vec{G}} e^{i\vec{G}\cdot\vec{r}}$, and denote $\tilde{\theta}_{\vec{G}-\vec{G}'} \equiv A_{\vec{G},\vec{G}'}$. Using $E_{\omega}(\vec{r}) = e^{i\vec{k}\cdot\vec{r}} u(\vec{r}) = \sum_{\vec{G}} \tilde{u}(\vec{G}) e^{i\vec{G}\cdot\vec{r}}$ a periodic function of the direct lattice (Bloch's theorem [31]), Eq. (4) becomes [13]

$$\sum_{\vec{G}'} \left(\delta_{\vec{G},\vec{G}'} (\vec{k} + \vec{G}) \cdot (\vec{k} + \vec{G}') + \frac{\omega_p^2}{c^2} A_{\vec{G},\vec{G}'} \right) \tilde{u}(\vec{G}') = \frac{\omega^2}{c^2} \epsilon_b \tilde{u}(\vec{G}). \quad (\text{A1})$$

Solutions $\{\psi_{\vec{k},l}(\vec{r})\}$ of the Hermitian eigenvalue problem Eq. (A1), corresponding to eigenvalues $\{\omega_{\vec{k},l}\}$, form a complete set of functions in the Hilbert space of Eq. (4). We write $\psi_{\vec{k},l}(\vec{r}) = (e^{i\vec{k}\cdot\vec{r}} / \alpha_{\vec{k},l}) u_{\vec{k},l}(\vec{r})$ and we choose the (real) normalization constant $\alpha_{\vec{k},l}$ such that

$$\frac{1}{\mathcal{V}} \int_{\mathcal{V}} d^2r \psi_{\vec{k},l}^*(\vec{r}) \psi_{\vec{k},l}(\vec{r}) \epsilon_{\vec{k},l}(\vec{r}) = 1, \quad (\text{A2})$$

where $\epsilon_{\vec{k},l}(\vec{r}) \equiv \epsilon_b - (\omega_p^2 / \omega_{\vec{k},l}^2) \theta(\vec{r})$. Using $u_{\vec{k},l}(\vec{r}) = \sum_{\vec{G}'} \tilde{u}_{\vec{k},l}(\vec{G}') e^{i\vec{G}'\cdot\vec{r}}$ and $\int_{\mathcal{V}} d^2r e^{i\vec{G}\cdot\vec{r}} = \mathcal{V}_0 \delta_{\vec{G},0}$, the normalization condition becomes

$$\sum_{\vec{G},\vec{G}'} \tilde{u}_{\vec{k},l}^*(\vec{G}) \tilde{u}_{\vec{k},l}(\vec{G}') \left(\epsilon_b \delta_{\vec{G},\vec{G}'} - \frac{\omega_p^2}{\omega_{\vec{k},l}^2} A_{\vec{G},\vec{G}'} \right) = \alpha_{\vec{k},l}^2. \quad (\text{A3})$$

From Eq. (A1) we obtain

$$\begin{aligned} \sum_{\vec{G},\vec{G}'} \tilde{u}_{\vec{k},l}^*(\vec{G}) \tilde{u}_{\vec{k},l}(\vec{G}') \left(\epsilon_b \delta_{\vec{G},\vec{G}'} - \frac{\omega_p^2}{\omega_{\vec{k},l}^2} A_{\vec{G},\vec{G}'} \right) \\ = \frac{c^2}{\omega_{\vec{k},l}^2} \sum_{\vec{G}} (\vec{k} + \vec{G})^2 \tilde{u}^*(\vec{G}) \tilde{u}(\vec{G}). \end{aligned} \quad (\text{A4})$$

Comparing Eq. (A3) and Eq. (A4) we obtain

$$\alpha_{\vec{k},l}^2 = \frac{c^2}{\omega_{\vec{k},l}^2} \sum_{\vec{G}} (\vec{k} + \vec{G})^2 |\tilde{u}_{\vec{k},l}(\vec{G})|^2. \quad (\text{A5})$$

- [1] S. John, Phys. Rev. Lett. **53**, 2169 (1984).
- [2] S. John, Phys. Rev. Lett. **58**, 2486 (1987).
- [3] E. Yablonovitch, Phys. Rev. Lett. **58**, 2059 (1987).
- [4] V. P. Bykov, Sov. J. Quantum Electron. **4**, 861 (1975).
- [5] S. John and J. Wang, Phys. Rev. Lett. **64**, 2418 (1990).
- [6] S. John and T. Quang, Phys. Rev. A **50**, 1764 (1994).
- [7] S. John and T. Quang, Phys. Rev. Lett. **78**, 1888 (1997).
- [8] R. Wang and S. John, Phys. Rev. A **70**, 043805 (2004).
- [9] J. G. Fleming, S. Y. Lin, I. El-Kady, R. Biswas, and K. M. Ho, Nature (London) **417**, 52 (2002).
- [10] S. Y. Lin, J. Moreno, and J. G. Fleming, Appl. Phys. Lett. **83**, 380 (2003).
- [11] S. Y. Lin, J. Moreno, and J. G. Fleming, Opt. Lett. **28**, 1909 (2003).
- [12] F. Wooten, *Optical Properties of Solids* (Academic Press, New York, 1972).
- [13] V. Kuzmiak, A. A. Maradudin, and F. Pincemin, Phys. Rev. B **50**, 16835 (1994).
- [14] G. von Freymann, S. John, M. Schulz-Dobrick, E. Vekris, N. Tétreault, S. Wong, V. Kitaev, and G. A. Ozin, Appl. Phys. Lett. **84**, 224 (2004).
- [15] O. Toader and S. John, Phys. Rev. E **70**, 046605 (2004).
- [16] A. Kubo, N. Pontius, and H. Petek, Nano Lett. **7**, 470 (2007).
- [17] A. Kubo, K. Onda, H. Petek, Z. Sun, Y. S. Jung, and H. K. Kim, Nano Lett. **5**, 1123 (2005).
- [18] H. Sai, Y. Kanamori, and H. Yugami, J. Microchem. Microeng. **15**, S243 (2005).
- [19] A. Kaso and S. John, Phys. Rev. E **74**, 046611 (2006).
- [20] *Handbook of Optical Constants of Solids*, edited by E. D. Palik (Academic Press, New York, 1985).
- [21] A. Yariv, *An Introduction to Theory and Applications of Quantum Mechanics* (John Wiley & Sons, New York, 1982).
- [22] K. L. Silverman, R. P. Mirin, S. T. Cundiff, and A. G. Norman, Appl. Phys. Lett. **82**, 4552 (2003).
- [23] P. G. Eliseev, H. Li, A. Stintz, G. T. Liu, T. C. Newell, K. J. Malloy, and L. F. Lester, Appl. Phys. Lett. **77**, 262 (2000).
- [24] F. W. Wise, Acc. Chem. Res. **33**, 773 (2000).
- [25] B. N. J. Persson and A. Baratoff, Phys. Rev. Lett. **68**, 3224 (1992).
- [26] M. Cox, Phys. Rev. **64**, 241 (1943).
- [27] M. A. Ordal, R. J. Bell, Jr., L. L. Long, and M. R. Querry, Appl. Opt. **24**, 4493 (1985).
- [28] J. H. Weaver, C. G. Olsoni, and D. W. Lynch, Phys. Rev. B **12**, 1293 (1975).
- [29] N. W. Ashcroft and N. D. Mermin, *Solid State Physics* (Saunders College Publishing, Philadelphia, 1976).
- [30] R. Wang and S. John (unpublished).
- [31] K. M. Ho, C. T. Chan, and C. M. Soukoulis, Phys. Rev. Lett. **65**, 3152 (1990).